Nanoscale

PAPER

View Article Online
View Journal | View Issue

Check for updates

Cite this: *Nanoscale*, 2018, **10**, 17182

Self-assembled vertically aligned Ni nanopillars in CeO_2 with anisotropic magnetic and transport properties for energy applications†

Jijie Huang,[a] Zhimin Qi,[a] Leigang Li,[a] Han Wang,[a] Sichuang Xue,[a] Bruce Zhang,[b] Xinghang Zhang[a] and Haiyan Wang *[a,b]

Received 9th July 2018,
Accepted 15th August 2018

DOI: 10.1039/c8nr05532g

rsc.li/nanoscale

Self-assembled vertically aligned metal–oxide (Ni–CeO_2) nanocomposite thin films with novel multifunctionalities have been successfully deposited by a one-step growth method. The novel nanocomposite structures presents high-density Ni-nanopillars vertically aligned in a CeO_2 matrix. Strong and anisotropic magnetic properties have been demonstrated, with a saturation magnetization (M_s) of ~175 emu cm^{-3} and ~135 emu cm^{-3} for out-of-plane and in-plane directions, respectively. Such unique vertically aligned ferromagnetic Ni nanopillars in the CeO_2 matrix have been successfully incorporated in high temperature superconductor $YBa_2Cu_3O_7$ (YBCO) coated conductors as effective magnetic flux pinning centers. The highly anisotropic nanostructures with high density vertical interfaces between the Ni nanopillars and CeO_2 matrix also promote the mixed electrical and ionic conductivities out-of-plane and thus demonstrate great potential as nanocomposite anode materials for solid oxide fuel cells and other potential applications requiring anisotropic ionic transport properties.

Introduction

A multifunctional two-phase vertically aligned nanocomposite (VAN) provides a great opportunity to achieve extraordinary properties arising from the two phases and their highly strained vertical heterointerfaces.[1–3] The design potential of VAN systems towards desirable properties are enormous, given the large selection of materials and the two-phase combinations. Most of the VAN demonstrations are oxide–oxide systems with the goal of either enhanced physical properties or combined functionalities through two-phase coupling. For example, tunable band structures,[4] vertical exchange bias,[5] multiferroics,[6] magnetoresistance,[7,8] novel anisotropic electronic-ionic transport,[9,10] and coupled extraordinary dielectric and optical performance[11,12] have been demonstrated in various oxide–oxide VAN systems. The growth mechanisms for different 2-phase oxide–oxide systems have also been explored,[1] which are correlated with various morphologies observed, including nanocheckerboard structures,[11,13] nanopillars in matrix,[14,15] and 2-phase domain structures.[16]

Very different from oxide–oxide VAN systems, metal–oxide VAN systems with vertically aligned metal nanopillars embedded in an oxide matrix provide another large group of materials (*i.e.*, metals) and novel functionalities in the VAN designs. For example, metal–oxide nanocomposite systems are considered as hybrid metamaterials for novel plasmonic and optical properties. Currently, electrochemical deposition on a porous alumina template[17,18] and complicated nanofabrication approaches such as combined focus ion beam (FIB) and electroplating,[19] electron beam lithography,[20] and electron beam evaporation[21] are mostly involved in the synthesis of such metal–oxide hybrid materials. The costly template and tedious nanofabrication methods limit the further scale-up processing for applications; in addition, it is challenging to obtain ultra-fine metal pillars (≤10 nm) by these methods. To overcome these challenges, a one-step PLD method has been demonstrated to grow self-assembled metal–oxide VAN systems with high epitaxial quality.[22,23] For example, Co–$BaZrO_3$ (BZO) nanocomposite thin films have been deposited with Co nanopillars embedded in a BZO matrix, and the pillar size can be tailored by changing the deposition frequency.[22] Some of the metal–oxide nanocomposites were also later realized by a magnetron sputtering technique.[24] Compared to the relatively easy growth of oxide–oxide VANs, challenges emerge to achieve metal–oxide VANs, due to the completely different growth kinetics for metals and oxides, as well as different surface energies and

[a]School of Materials Engineering, Purdue University, West Lafayette, IN, 47906 USA. E-mail: hwang00@purdue.edu
[b]School of Electrical and Computer Engineering, Purdue University, West Lafayette, IN, 47906 USA

† Electronic supplementary information (ESI) available. See DOI: 10.1039/c8nr05532g

wetting properties on substrates, and possible inter-diffusion.

To overcome these challenges, careful material selection and growth condition optimization are essential. In this study, we selected a face-centered cubic (fcc) metal, Ni and a cubic (fluorite) oxide, CeO_2, as the two phases. The expected structure is illustrated in Fig. 1a, showing a VAN structure of Ni nanopillars embedded in a CeO_2 matrix. The interest in this metal–oxide system is due to the anisotropic magnetic Ni nanopillars, as well as the anisotropic ionic and electrical conductivities of Ni–CeO_2 nanocomposites. Taking advantage of the anisotropic nature of the magnetic Ni nanopillars, various applications are envisioned, such as high-density magnetic recording media and nanoscale magnetic flux pinning centers for high temperature superconducting thin films. For example, in terms of magnetic flux pinning properties, the magnetic Ni nanopillars in this case are expected to provide a magnetic pinning effect for superconducting $YBa_2Cu_3O_{1-x}$ (YBCO) thin films, and the CeO_2 matrix can effectively encapsulate Ni and minimize the possible inter-diffusion between the metal Ni and YBCO layer.[25–29] In this work, the Ni–CeO_2 nanolayer is introduced into YBCO as a cap layer to investigate its pinning effect. Furthermore, by including the conducting Ni metal pillars, the overall vertical conductivity of the film is enhanced and thus a highly anisotropic conductor is designed and demonstrated.

Results and discussion

The typical plan-view scanning transmission electron microscopy (STEM) image shown in Fig. 1b well captures the obvious Ni nanopillars with an average diameter of ~7 nm. Energy-dispersive X-ray spectral (EDS) mapping of a selected area was conducted to determine the two phases, Ni (Ni elemental mapping in Fig. 1c) and CeO_2 (Ce elemental mapping in Fig. 1d). The sharp interface between them suggests that there is very little or no intermixing between the metal and oxide phases in the nanocomposite film. In addition, the volume ratio of Ni nanopillars can be estimated to be ~55% based on multiple plane-view STEM images. Both Ni (002) and Ni (022) nanopillars can be identified in the high-resolution TEM image in Fig. 1e, as Ni (a = 3.524 Å) is not perfectly matched with the STO substrate (a = 3.905 Å) and thus presents two possible orientations. Cross-sectional STEM was then carried out to explore the 3-D nature of the composite film. It is obvious that the vertically self-assembled Ni nanopillars were grown throughout the entire thickness of the film, as shown in the low-magnification STEM image in Fig. 1f. The corresponding EDS mapping in Fig. 1g shows clear Ni nanopillars in the CeO_2 matrix with a clean out-of-plane interface. Furthermore, the surface of the film is relatively smooth, which can be further confirmed by the AFM image shown in Fig. S4† with a low surface roughness of R_q = 1.33 nm. Fig. 1h

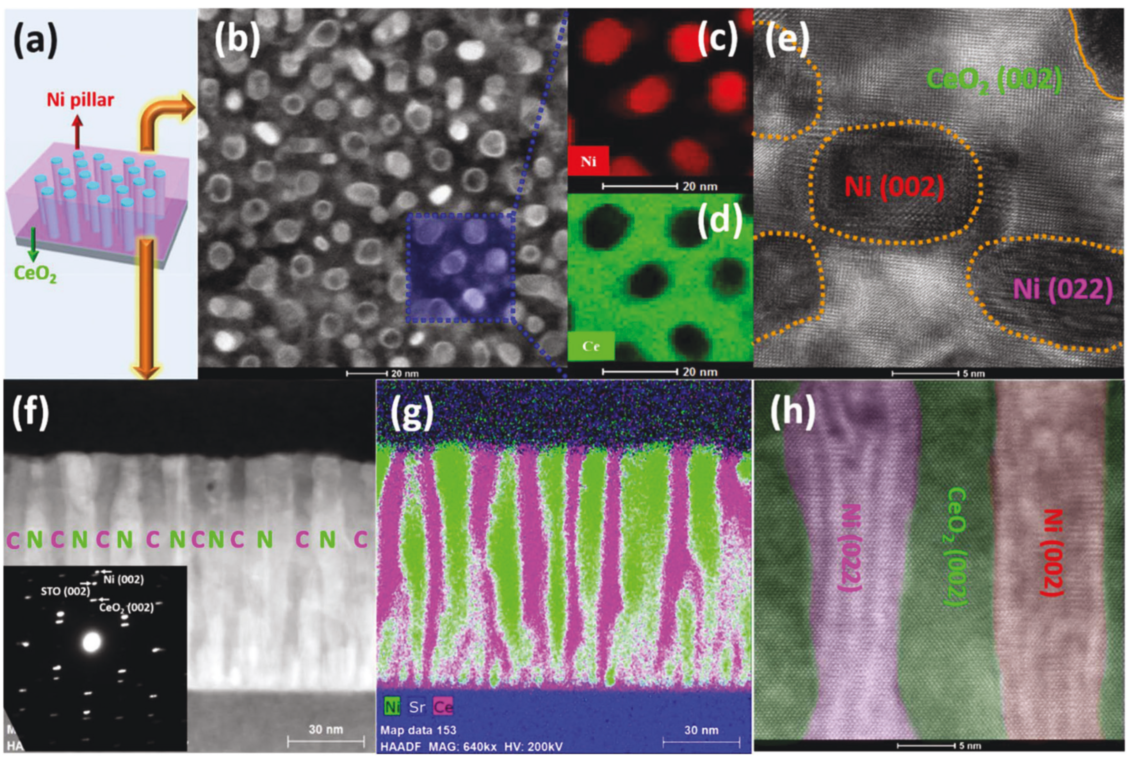

Fig. 1 Microstructure study of the Ni–CeO_2 film deposited on the STO substrate. (a) 3D schematic illustration of the film; (b) plan-view STEM image of a selected area of the film, with EDS mapping of (c) Ni and (d) Ce elements; (e) high resolution image to show the crystal structure of the pillars; (f) cross-sectional STEM image of a selected area of the film with the selected area electron diffraction (SAED) pattern and (g) its corresponding EDS mapping; (h) atomic-scale high resolution STEM image of a selected area with Ni pillars.

displays a high-resolution STEM image for a representative area with both Ni (002) and Ni (022) nanopillars, which further confirms the high film quality and no inter-mixing between Ni and CeO_2. It is also noted that the number of Ni (002) nanopillars is much greater than that of Ni (022) nanopillars. In addition, the ratio of Ni (002) and Ni (022) can be varied by controlling the growth conditions. A higher growth temperature of 750 °C results in more Ni (022) pillars as revealed in Fig. S3 in the ESI.†

To examine the crystal structure and determine the phases in this metal–oxide composite thin film, X-ray diffraction (XRD) analysis was conducted. CeO_2 has grown preferably in the (00*l*)-direction, as demonstrated by the standard θ–2θ XRD pattern in Fig. 2a. Consistent with the above TEM/STEM analysis, Ni nanopillars grow preferably along the (002) orientation (2θ = 51.637°) with some minor ones along the (022) orientation (2θ = 76.095°), evidenced from the Ni peak intensities. Tensile strain along (002) and (022) for Ni (002) and Ni (022) can be determined, compared to bulk Ni from PDF #04-0850, which might enhance the magnetic response of Ni.[30] As mentioned, Ni presents a face-centered cubic (fcc) structure with a lattice parameter of a_{Ni} = 3.524 Å, while the substrate STO has a perovskite structure with a lattice constant of a_{STO} = 3.905 Å. The lattice mismatch between Ni and STO is relatively high at 10.37% (calculated based on $f = (a_{STO} - a_{Ni})/\left(\frac{a_{STO} + a_{Ni}}{2}\right)$). Thus, an in-plane domain matching epitaxy (DME) is applied to satisfy the epitaxial growth of Ni on STO,[31] *i.e.*, 10 of $(002)_{Ni}$ match with 9 of $(002)_{STO}$. On the other hand, CeO_2 (a_{CeO_2} = 5.41134 Å) has a perfect lattice matching with STO after 45° rotation, which allows the lattice matching epitaxial (LME) growth. For the out-of-plane matching between CeO_2 and Ni, DME is implemented for both Ni (002) and Ni (022), because of the large lattice mismatch in both cases. As the surface energy of Ni (002) is lower than that of Ni (022), more Ni is anticipated to grow along the *c*-direction, which is evidenced from the stronger Ni (00*l*) peaks in the XRD scans. Furthermore, the φ-scans of Ni (111), CeO_2 (111) and STO (111) are shown in Fig. 2b to explore the in-plane matching of the film with the substrate. Interestingly, the Ni (111) scan shows an 8-fold pattern, which suggests the presence of two sets of structural domains inside Ni (002). Therefore, two in-plane epitaxial relationships can be identified, Ni [100]//STO [100], Ni [010]//STO [010], and Ni [110]//STO [100], Ni [$\bar{1}$10]//STO [010]. In addition, for the Ni (022) domains, the in-plane matching with the substrate follows Ni [100]//STO [100] and Ni [0$\bar{1}$1]//STO [010]. Furthermore, CeO_2 (111) peaks exhibit an excellent match with STO (111) peaks after a 45° rotation. Based on the XRD results, the overall growth relationships of the Ni–CeO_2 nanocomposite film and STO substrate are determined and illustrated by the atomic crystallographic images in Fig. 2c.

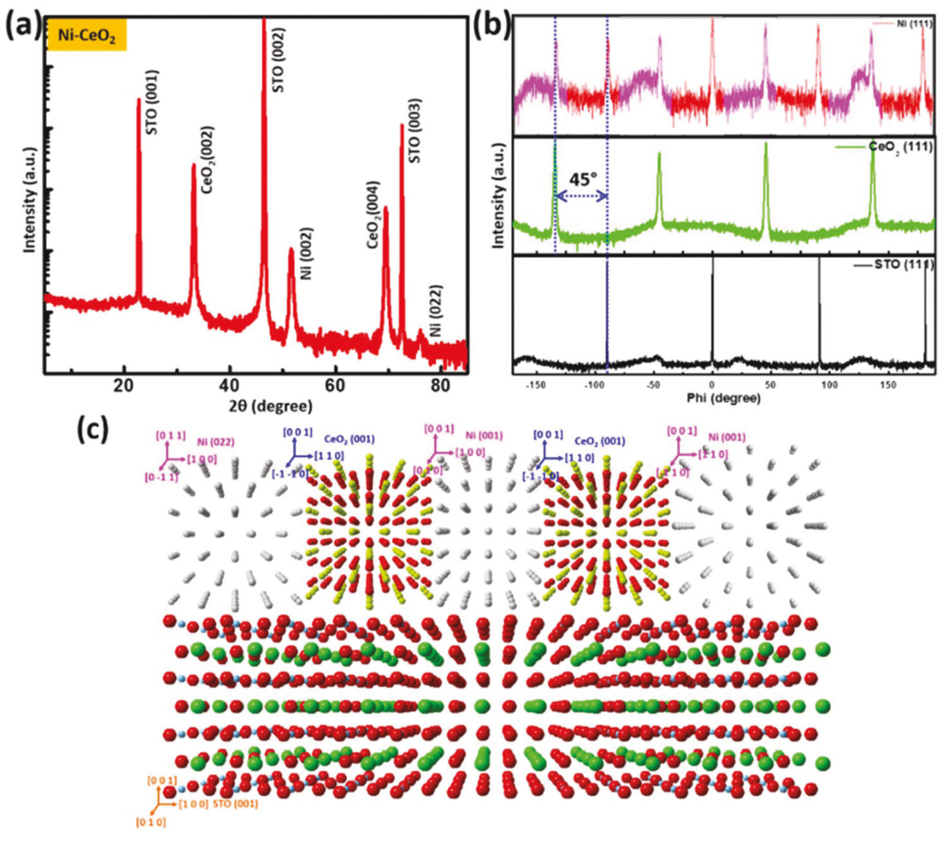

Fig. 2 (a) XRD θ–2θ pattern of the Ni–CeO_2 thin film grown on STO (001); (b) φ scan of STO (111), CeO_2 (111) and Ni (111) peaks; (c) crystallographic image to show the nanocomposite film built-up.

The epitaxial growth of the metal–oxide nanocomposite thin film with self-assembled Ni nanopillars in the CeO_2 matrix is quite interesting and thus worth further investigation. Similar to the intensively studied oxide–oxide VAN systems,[1–3] the growth mechanism of this metal–ceramic nanocomposite film follows two steps of nucleation and film growth. The surface energy for Ni (001), Ni (022), CeO_2 (001) and STO (001) is 2.426 J m^{-2}, 2.368 J m^{-2}, 1.0–1.4 J m^{-2}, and 1.26 J m^{-2}, respectively.[32–34] As a result, the higher interfacial energy (lower wettability) between Ni and STO (γ_{NS}) leads to the Volmer–Weber 3D island growth mode, which initiates 3D Ni island nucleation and forms nanopillars finally. However, for the growth of CeO_2, either the 2D Frank–van der Merwe mode or the 2D + 3D Stranski–Krastanov mode is dominant because of its lower interfacial energy γ_{CS} (higher wettability) with STO, which results in a layer-by-layer growth to form the overall matrix. The corporative growth of Ni and CeO_2 following their independent growth modes allows the formation of such a metal–oxide VAN structure with Ni nanopillars embedded in the CeO_2 matrix. This one-step PLD method can also be applied to many other metal–oxide systems, for example an epitaxial Ni–$BaTiO_3$ (BTO) system has also been successfully grown, as presented by microstructure characterization in Fig. S1.†

Nanostructured magnetic materials are promising for various technological applications, such as magnetic data storage. Taking advantage of these self-assembled vertical Ni nanopillars, it is essential to explore the magnetic properties of these high density anisotropic nanopillars. The M–H measurements at different temperatures were carried out for Ni–CeO_2 nanocomposite films, and the hysteresis loops are shown in Fig. 3a for in-plane (IP: the applied magnetic field parallel to the film surface) and in Fig. 3b for out-of-plane (OP: the applied magnetic field perpendicular to the film surface), respectively. The inserted figures are the enlarged area of the orange squares, which can be used to determine its coercivity (H_c) at different temperatures. As seen from the H_c *vs.* temperature plot in Fig. 3c, the H_c value decreases with increasing temperature, along both IP and OP directions, which suggests a thermally activated magnetization reversal process, as well as the existence of magnetic anisotropy of the Ni–CeO_2 nanocomposite film. As the temperature increases, thermal fluctuations or thermal perturbations could reduce the coercivity, which has been observed in various other magnetic materials.[35,36] The magnetic anisotropy can be clearly revealed by the *M–H* curves (at 300 K) comparing the IP and OP measurements as shown in Fig. 3d. The saturation magnetization (M_s) is ~175 emu cm^{-3} and ~135 emu cm^{-3} for OP and

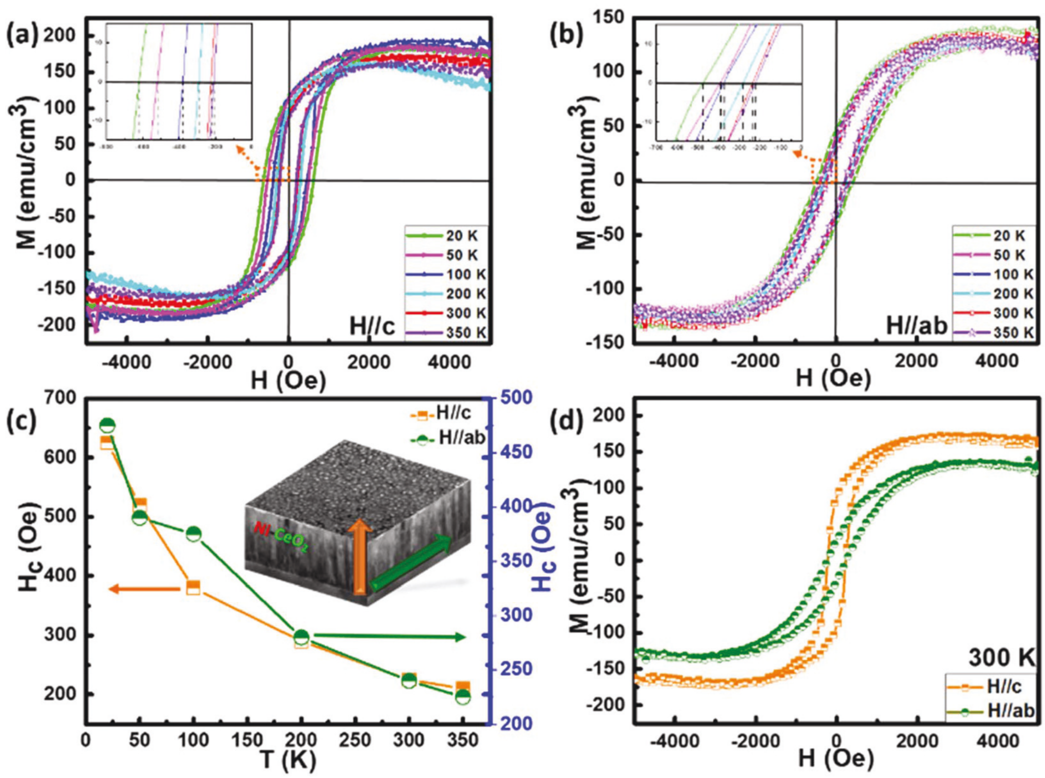

Fig. 3 The magnetic hysteresis loops for the Ni–CeO_2 film at varying temperatures with an applied magnetic field (a) parallel or (b) perpendicular to the film surface, and the insets are the enlargement of the marked area to identify coercivity values; (c) coercivity values as a function of the measured temperature; (d) in-plane and out-of-plane *M–H* curve comparison of the sample at room temperature to show its anisotropic magnetic performance.

IP, respectively. It is worth noting that the entire nanocomposite volume (including both the Ni nanopillars and the CeO_2 matrix) is taken into account. When considering the actual volume density of the magnetic Ni nanopillars in the overall film (~55%), the M_s value can be as high as ~320 emu cm^{-3} for OP and ~245 emu cm^{-3} for IP. The M_s values are lower than that of 420 emu cm^{-3} for bulk Ni,[37] which is possibly due to the very fine Ni nanopillars and the orientations of the Ni nanopillars ([001] and [022]) which are not along the easy axis of Ni [111]. It is noted that the field applied might not be strong enough to align all the magnetic dipoles in the hard magnetization direction. In this case, the magnetic anisotropy of the Ni nanopillars can be considered to be from the competition between magneto-crystalline anisotropy and shape anisotropy, if the interaction between the Ni nanopillars is ignored. As the growth directions of the Ni nanopillars are [001] and [022] in this case, there is an angle of 54.73° and 35.27° with the magneto-crystalline easy axis of [111]. Therefore, the shape anisotropy is considered as the dominating factor for the magnetic anisotropy in Ni nanopillars. In addition, the temperature-dependence of magnetization of Ni–CeO_2 was measured up to 380 K (due to the limitation of the PPMS tool) with an applied magnetic field perpendicular to the film surface, as shown in Fig. S2.† As shown, the magnetization does not disappear up to 380 K, which is because the Curie temperature of Ni is 627 K.

As mentioned above, magnetic nanostructures could provide a magnetic flux pinning effect for high temperature superconductors to achieve better in-field superconducting properties (especially the in-field critical current density $J_c^{\text{in-field}}$). Therefore, this nanocomposite thin film with high-density magnetic Ni nanopillars could be an ideal candidate for the magnetic pinning effect. As a demonstration, a thin layer of the Ni–CeO_2 VAN was incorporated into YBCO for flux pinning enhancement, as illustrated in the schematic drawing in Fig. 4a. The magnetic Ni nanopillars act as effective magnetic flux pinning centers, while the CeO_2 matrix effectively encapsulates the Ni nanopillars and minimizes the inter-diffusion between the YBCO and Ni. The microstructure study in Fig. S5† confirms that no or very limited inter-diffusion exists between the YBCO layer and Ni–CeO_2 layer on top. Superconducting properties (*e.g.*, transition temperature T_c and critical current density J_c) are measured for YBCO thin films, with or without the Ni–CeO_2 nanocomposite layer. First, the *R*–*T* property was measured and plotted in Fig. 4b. The inserted plot is the enlarged transition regime to determine the T_c values. The results show that the temperature where the resistivity goes to absolute zero (T_c^{zero}) is 86.5 K for the doped YBCO and 89 K for pure YBCO, which is comparable to previous reports.[26–29,38,39] The slight T_c drop of the YBCO with the Ni–CeO_2 layer might result from the incorporation of the Ni–CeO_2 nanocomposite layer. More importantly, the J_c values were also measured and compared at 77 K (Fig. 4c) and 65 K (Fig. 4d), with the applied magnetic field perpendicular to the film surface (H//c). Under a low applied field, the J_c value of pure YBCO is higher, while the J_c–H curve becomes flatter for

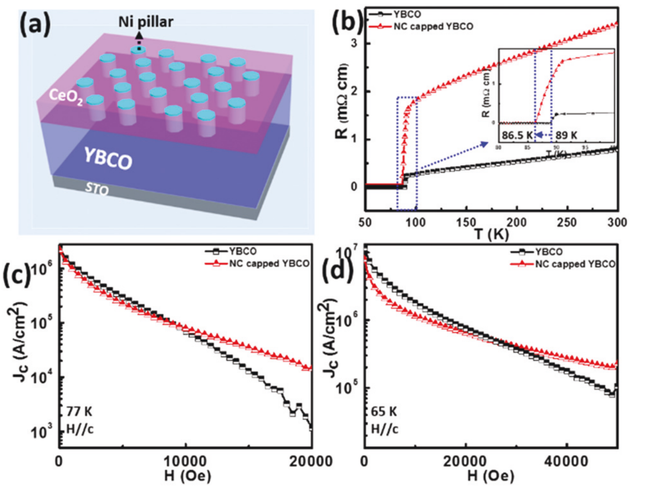

Fig. 4 (a) Schematic illustration of the nanocomposite capped YBCO film; (b) *R*–*T* plots of YBCO thin films, with or without the Ni–CeO_2 nanocomposite layer, the inserted figure is the enlargement around the transition temperature regime; the in-field critical current density dependence of the applied magnetic field for both films at (c) 77 K and (d) 65 K.

Ni–CeO_2 (NC) capped YBCO with increasing field. And, the absolute value of J_c of Ni–CeO_2-capped YBCO exceeds pure YBCO at higher fields beyond 1 T and 2.5 T, for 77 K and 65 K, respectively. This suggests that the magnetic pinning is effectively introduced by the Ni–CeO_2 nanocomposite in the high field regime. The results demonstrate the effective pinning enhancement by the Ni–CeO_2 nanocomposite, especially at high fields, which indicates the potential high field applications of YBCO with the Ni–CeO_2 nanocomposite. In such a scheme, a magnetic pinning force is generated by the interaction between the magnetic Ni nanopillars and the magnetic flux in the vertices of YBCO, which accordingly requires larger Lorentz force to move the normal cores. Therefore, magnetic pinning is provided by the magnetic Ni nanopillars.

To explore the anisotropic transport properties of the unique Ni–CeO_2 nanocomposite thin film, AC impedance measurement was carried out, in both IP and OP directions. The EIS data in Fig. S6† of both OP and IP directions prove that the incorporation of Ni metal in the CeO_2 matrix greatly reduces the resistance compared to pure CeO_2. The IP data for both Ni–CeO_2 and pure CeO_2 are shown in Fig. S6a,† and the Ni–CeO_2 nanocomposite presents a much smaller semicircle than that of the pure CeO_2. Both CeO_2 films, with or without Ni nanopillars, show a similar single semi-circle characteristic instead of two semi-circles as seen in the cases of bulk materials, which is believed to be caused by the large stray capacitance from the substrate.[38] For the OP measurement in Fig. S6b,† the Ni–CeO_2 composite shows the behavior of an inductor because of the highly conductive nature since metallic Ni is vertically aligned throughout the entire film and becomes the preferred conduction paths. Besides, the second component in the low frequency regime represents the electrode effect.[40] The incomplete semi-circle in the high frequency regime is due to the limitation of the impedance analyser used. Overall, the unique Ni–CeO_2 vertically aligned nanocomposite film presents a highly anisotropic transport property.

Conclusions

The self-assembled Ni–CeO_2 nanocomposite thin films have been successfully grown by a one-step PLD method, under carefully controlled growth conditions. From the microstructure study, high density ultra-fine Ni nanopillars of ~7 nm embedded in the CeO_2 matrix have been successfully demonstrated. High epitaxial quality of both phases has been demonstrated with sharp interface. The metal–oxide nanocomposite films with anisotropic magnetic properties (*i.e.*, the preferred OP magnetization) have been incorporated into a superconducting YBCO thin film as a cap layer. Enhanced flux pinning properties in the doped YBCO film have been demonstrated compared to pure YBCO thin films, especially in the high magnetic field regime. Highly anisotropic electrical and ionic conductivities in Ni–CeO_2 nanocomposite thin films could also be ideal for the thin film anode structure in SOFCs. This unique anisotropic metal–oxide nanocomposite thin film could find promising applications in high-density magnetic data storage and magnetic tunnel junction devices.

Conflicts of interest

There are no conflicts to declare.

Acknowledgements

J. H. and H. W. acknowledge the support from the Basil S. Turner Chair Professorship at Purdue University for the seminal work. X. S., Han W., B. Z. and H. W. acknowledge the support from the U.S. National Science Foundation (Ceramic Program, DMR-1565822 for high resolution STEM and DMR-1809520 for thin film growth).

References

1 J. L. MacManus-Driscoll, *Adv. Funct. Mater.*, 2010, **20**, 2035–2045.
2 H. Y. Hwang, Y. Iwasa, M. Kawasaki, B. Keimer, N. Nagaosa and Y. Tokura, *Nat. Mater.*, 2012, **11**, 103.
3 J. Huang, J. L. MacManus-Driscoll and H. Wang, *J. Mater. Res.*, 2017, **32**(21), 4054.
4 W. Chang, H. Liu, V. Tra, J. Chen, T. Wei, W. Y. Tzeng, Y. Zhu, H. Kuo, Y. Hsieh, J. Lin, Q. Zhan, C. Luo, J. Lin, J. He, C. Wu and Y. Chu, *ACS Nano*, 2014, **8**(6), 6424–6429.
5 J. Huang, A. Gellatly, A. Kauffmann, X. Sun and H. Wang, *Cryst. Growth Des.*, 2018, **18**, 4388–4394.
6 H. Zheng, J. Wang, S. E. Lofland, Z. Ma, L. Mohaddes-Ardabili, T. Zhao, L. Salamanca-Riba, S. R. Shinde, S. B. Ogale, F. Bai, D. Viehland, Y. Jia, D. G. Schlom, M. Wuttig, A. Roytburd and R. Ramesh, *Science*, 2004, **303**, 661.
7 M. Fan, B. Zhang, H. Wang, J. Jian, X. Sun, J. Huang, L. Li, X. Zhang and H. Wang, *Adv. Mater.*, 2017, **29**, 1606861.
8 A. Chen, Z. Bi, C.-F. Tsai, J. Lee, Q. Su, X. Zhang, Q. Jia, J. L. MacManus-Driscoll and H. Wang, *Adv. Funct. Mater.*, 2011, **21**, 2423.
9 Y. H. Hsieh, J. M. Liou, B. C. Huang, C. W. Liang, Q. He, Q. Zhan, Y. P. Chiu, Y. C. Chen and Y. H. Chu, *Adv. Mater.*, 2012, **24**, 4564.
10 S. Lee, A. Sangle, P. Lu, A. Chen, W. Zhang, J. S. Lee, H. Wang, Q. Jia and J. L. MacManus-Driscoll, *Adv. Mater.*, 2014, **26**, 6284.
11 J. L. MacManus-Driscoll, P. Zerrer, H. Wang, H. Yang, J. Yoon, A. Fouchet, R. Yu, M. G. Blamire and Q. Jia, *Nat. Mater.*, 2008, **7**, 314.
12 H. J. Liu, L. Y. Chen, Q. He, C. W. Liang, Y. Z. Chen, Y. S. Chien, Y. H. Hsieh, S. J. Lin, E. Arenholz, C. W. Luo, Y. L. Chueh, Y. C. Chen and Y. H. Chu, *ACS Nano*, 2012, **6**, 6952.
13 S. Park, Y. Horibe, T. Asada, L. S. Wielunski, N. Lee, P. L. Bonanno, S. M. O'Malley, A. A. Sirenko, A. Kazimirov, M. Tanimura, T. Gustafsson and S. W. Cheong, *Nano Lett.*, 2008, **8**, 720.
14 H. M. Zheng, F. Straub, Q. Zhan, P. L. Yang, W. K. Hsieh, F. Zavaliche, Y. H. Chu, U. Dahmen and R. Ramesh, *Adv. Mater.*, 2006, **18**, 2747.
15 J. Huang, X. Wang, N. L. Hogan, S. Wu, P. Lu, Z. Fan, Y. Dai, B. Zeng, R. Starko-Bowes, J. Jian, H. Wang, L. Li, R. Prasankumar, D. Yarotski, M. Sheldon, H. Chen, Z. Jacob, X. Zhang and H. Wang, *Adv. Sci.*, 2018, 1800416.
16 A. Goyal, S. Kang, K. J. Leonard, P. M. Martin, A. A. Gapud, M. Varela, M. Paranthaman, A. O. Ijaduola, E. D. Specht, J. R. Thompson, D. K. Christen, S. J. Pennycook and F. A. List, *Supercond. Sci. Technol.*, 2005, **18**, 1533.
17 J. Yao, Z. W. Liu, Y. M. Liu, Y. Wang, C. Sun, G. Bartal, A. M. Stacy and X. Zhang, *Science*, 2008, **321**(5891), 930.
18 A. V. Kabashin, P. Evans, S. Pastkovsky, W. Hendren, G. A. Wurtz, R. Atkinson, R. Pollard, V. A. Podolskiy and A. V. Zayats, *Nat. Mater.*, 2009, **8**, 867.
19 J. K. Gansel, M. Thiel, M. S. Rill, M. Decker, K. Bade, V. Saile, G. von Freymann, S. Linden and M. Wegener, *Science*, 2009, **325**(5947), 1513.
20 N. A. Melosh, A. Boukai, F. Diana, B. Gerardot, A. Badolato, P. M. Petroff and J. R. Heath, *Science*, 2003, **300**, 112–115.
21 N. A. Melosh, A. Boukai, F. Diana, B. Gerardot, A. Badolato, P. M. Petroff and J. R. Heath, *Science*, 2003, **300**(5616), 112.
22 J. Huang, L. Li, P. Lu, Z. Qi, X. Sun, X. Zhang and H. Wang, *Nanoscale*, 2017, **9**, 7970.
23 L. Li, L. Sun, J. S. Gomez-Diaz, N. L. Hogan, P. Lu, F. Khatkhatay, W. Zhang, J. Jian, J. Huang, Q. Su, M. Fan, C. Jacob, J. Li, X. Zhang, Q. Jia, M. Sheldon, A. Alú, X. Li and H. Wang, *Nano Lett.*, 2016, **16**, 3936–3943.

24 J. Gao, X. Wu, Q. Li, S. Du, F. Huang, L. Liang, H. Zhang, F. Zhuge, H. Cao and Y. Song, *Adv. Mater.*, 2017, **29**, 1605324.
25 J. Huang, L. Chen, J. Jian, K. Tyler, L. Li, H. Wang and H. Wang, *J. Phys.: Condens. Matter.*, 2016, **28**, 025702.
26 J. Huang, M. Fan, H. Wang, L. Chen, C. Tsai, L. Li and H. Wang, *Ceram. Int.*, 2016, **42**, 12202.
27 C. Tsai, J. Huang, J. Lee, F. Khatkhatay, L. Chen, A. Chen, Q. Su and H. Wang, *Physica C*, 2015, **510**, 13.
28 J. Huang, C. Tsai, L. Chen, J. Jian, F. Khatkhatay, K. Yu and H. Wang, *J. Appl. Phys.*, 2014, **115**, 123902.
29 J. Huang and H. Wang, *Supercond. Sci. Technol.*, 2017, **30**, 114004.
30 S. Manna, J. W. Kim, M. V. Lubarda, J. Wingert, R. Harder, F. Spada, V. Lomakin, O. Shpyrko and E. E. Fullerton, *AIP Adv.*, 2017, **7**, 125025.
31 J. Narayan and B. C. Larson, *J. Appl. Phys.*, 2003, **93**, 278–285.
32 L. Vitos, A. V. Ruban, H. L. Skriver and J. Kollar, *Surf. Sci.*, 1998, **411**, 186–202.
33 S. Hayun, S. V. Ushakov and A. Navrotsky, *J. Am. Ceram. Soc.*, 2011, **94**, 3679–3682.
34 B. Meyer, J. Padilla and D. Vanderbilt, *Faraday Discuss.*, 1999, **114**, 395–405.
35 S. Okamoto, R. Goto, N. Kikuchi, O. Kitakami, T. Akiya, H. Sepehri-Amin, T. Ohkubo, K. Hono, K. Hioki and A. Hattori, *J. Appl. Phys.*, 2015, **118**, 223903.
36 Y. Zhang, X. Li, J. Jing, X. Zhang and Y. Zhao, *J. Magn. Magn. Mater.*, 2016, **408**, 228–232.
37 J. H. Hwang, V. P. Dravid, M. H. Teng, J. J. Host, B. R. Elliott, D. L. Johnson and T. O. Mason, *J. Mater. Res.*, 1997, **12**, 1076–1082.
38 J. Huang, C. Tsai, L. Chen, J. Jian, K. Yu, W. Zhang and H. Wang, *IEEE Trans. Appl. Supercond.*, 2015, **25**(3), 7500404.
39 J. Huang, L. Li, X. Wang, Z. Qi, M. A. P. Sebastian, T. J. Haugan and H. Wang, *IEEE Trans. Appl. Supercond.*, 2017, **27**(4), 8000305.
40 N. W. Kwak and W. C. Jung, *Acta Mater.*, 2016, **108**, 271–278.